

# A New Computational Framework for UAV Quadrotor Noise Prediction

*Ana Vieira*  
*R&D Engineer*

*CEIIA, Porto, 4470-605 Maia, Portugal*

*Luís Cruz*  
*Aeroacoustics Engineer*

*CEIIA, Porto, 4470-605 Maia, Portugal*

*Fernando Lau*  
*Assistant Professor*

*IST, 1049-001 Lisbon, Portugal*

*João Pedro Mortágua*  
*R&D Manager*

*CEIIA, Porto, 4470-605 Maia, Portugal*

*Rui Santos*  
*R&D Manager*

*IST, 1049-001 Lisbon, Portugal*

## ABSTRACT

The sustainability of the forthcoming air traffic growth is seriously compromised by high levels of noise emission, a well-known hazard to human health. Rotating surfaces, such as rotors and propellers, are the most significant source of noise in aerial vehicles and adequate modelling methods are important enablers in the noise footprint optimization process. The computational procedure proposed is composed by CEIIA's in-house aerodynamics and aeroacoustics tools, which make use of parallel computing to accelerate the simulations. The procedure was successfully validated for helicopter noise and is now applied to Unmanned Aerial Vehicle (UAV) quadrotor noise due to their progressive importance both in military and civil actions. Exhaustive experimental tests in the controlled environment of an anechoic room were performed in order to obtain reliable experimental data. The present work describes the numerical and experimental framework for UAV quadrotor noise prediction and the correlation between experimental data and numerical results.

## NOMENCLATURE

$\delta$	Boundary layer
$\delta(f)$	Dirac delta function
$\nu$	Kinematic viscosity
$\rho_0$	Density in the undisturbed medium
$\tau$	Source time
$\tau_e$	Retarded time
$b$	Blade span
$c$	Speed of sound
$l_i$	Local force intensity, $l_i = p_{ij}n_j$
$M_r$	Mach number in the radiation direction
$M_T$	Rotor tip Mach number
$n_i$	Normal to the surface
$p_L$	Loading noise
$p_T$	Thickness noise
$p_{ij}$	Compressive stress tensor
$r$	Distance between source and observer
$S$	Surface area
$t$	Observer time
$T_{ij}$	Lighthill stress tensor

$u_i$	Local fluid velocity
$V$	Relative velocity
$v_i$	Local surface velocity
$v_n$	Velocity in the direction of the normal to the surface
$x_i$	Observer position
$y_i$	Source position

## 1 INTRODUCTION

The high level of noise generated during flight is a major concern for the aeronautical industry both in civil and military applications. If a quieter aircraft in a military field implies a higher survival rate, in the case of civil applications noise has a more comprehensive range of applications due to the sustainability of air traffic growth.

Over the last decades, significant effort has been dedicated to the study of noise modelling and reduction technologies. Although many improvements were carried out on commercial aircraft and rotorcraft in terms of noise reduction, these topics remain a challenge still today due to the distinct sources of noise in different aerial vehicles.

Rotor noise assumed importance since the 60's, a period marked for the first theoretical and experimental studies although limited by the lack of computer resources and understanding of the blade pressure distribution. A review of helicopter noise prediction is given by Brentner and Farassat<sup>1</sup>.

The Ffowcs Williams and Hawkings (FW-H) equation<sup>2</sup> and Kirchhoff equations<sup>3</sup> led to important advances in rotor noise prediction, as well as the subsequently formulations of Farassat<sup>4;5</sup>.

The evolution of computer power in recent years, together with an accurate description of the blade loading distribution, contributed to the development of sophisticated acoustic tools<sup>6;7</sup>. However, there are still several subjects requiring further study, as the noise generated in transient maneuvers<sup>8</sup>.

The emergence of new types of aerial vehicles, in the form of unmanned aerial vehicles (UAVs), poses a new challenge in terms of noise reduction<sup>9;10</sup>. Noise is particularly relevant in tactical UAVs<sup>11</sup>, making them easily detectable targets, which increases the probability of failure of a mission.

In UAVs with electric propulsion system, the propeller or rotor contributes significantly to the total noise, since they are designed taking into account performance results and neglecting the aeroacoustic behaviour.

This work presents a new acoustic tool, already validated for helicopter steady and unsteady flight, which is now applied to the prediction of a quadrotor UAV noise. In the absence of experimental data in the literature, an experimental setup was defined to validate the numerical analysis.

## 2 BACKGROUND

### 2.1 Rotor Noise

Rotor noise is defined by tonal and broadband noise components. The tonal noise is composed by thickness and loading noise, high-speed impulsive (HSI) noise and blade-vortex interaction (BVI) noise. The broadband noise is related with non-deterministic loading sources (e.g. blade-wake interaction noise, blade self-noise and turbulence ingestion noise).

Thickness noise is significant in hover and forward flight, resulting from the displacement of the fluid as the blade passes. This type of noise propagates along the rotor disk plane.

Loading noise results from non-impulsive sources that are generated by the accelerating force on the fluid as the blade passes. Loading noise is usually the dominant source of noise and its propagation direction is below the rotor disk plane.

HSI noise is associated with transonic flight conditions (with advancing tip Mach numbers above  $M_T = 0.85$ ), and is generated by shock waves in the flow field around the rotor, propagating in the same direction as the thickness noise.

BVI noise is a significant source of noise in descent and hover flight, and is produced by the interaction between a shed tip vortex with the following blades.

Broadband noise results from random fluctuations of the forces on the blade, caused by turbulence. One significant type of broadband noise is the rotor turbulent boundary layer, in particular, its interaction with the blade trailing edge.

## 2.2 Acoustic Analogy

The Ffowcs Williams-Hawkings (FW-H) equation is based on the Lighthill's acoustic analogy and it is an exact rearrangement of the continuity equation of the Navier-Stokes equations into the form of an inhomogeneous wave equation,

$$\left(\frac{\partial^2}{\partial t^2} - c^2 \frac{\partial^2}{\partial x_i^2}\right)(\overline{\rho} - \rho_0) = \frac{\partial}{\partial t}[\rho_0 v_n \delta(f)] - \frac{\partial}{\partial x_i}[p_{ij} n_j \delta(f)] + \frac{\partial^2 \overline{T}_{ij}}{\partial x_i \partial x_j}, \quad (1)$$

where  $\overline{T}_{ij}$  is a generalized function equal to Lighthill's stress tensor  $\overline{T}_{ij} = \rho u_i u_j + p_{ij} - c^2(\rho - \rho_0)\delta_{ij}$  outside any surfaces and equal to zero within them.

The three terms in the left hand of Eq. 1 correspond, respectively, to a monopole responsible for thickness noise, a dipole for loading noise and a quadrupole term. The monopole and dipole terms are surface distributions of sources, and have been used for several years in rotor noise prediction because they only require the blade surface pressure, and lead to accurate analysis in subsonic conditions. The quadrupole source is a volume distribution of sources, requiring knowledge of the flow field around the blade. Despite its recognized importance<sup>5</sup> the quadrupole term is frequently neglected in rotor noise prediction due to high computational demands.

## 2.3 Formulation 1A of Farassat

The calculation of the quadrupole term of Eq. 1 requires volume integration and an accurate prediction of the flow field. For these reasons, the quadrupole term is not considered in formulation 1A of Farassat, and only the solution of the following two wave equations is required,

$$\square^2 p'_T = \frac{\partial}{\partial t}[\rho_0 v_n \delta(f)], \quad (2)$$

$$\square^2 p'_L = -\frac{\partial}{\partial x_i}[l_i \delta(f)], \quad (3)$$

where  $p'_T$  and  $p'_L$  are the pressure perturbation due to the thickness and loading noise, respectively, and  $l_i = p_{ij} n_j$ .

Eq. 2 and Eq. 3 result into the following final expressions for the thickness and loading noise:

$$p'_T(x, t) = \int_{f=0} \left[ \frac{\rho_0 \dot{v}_n}{r(1 - M_r)^2} \right] dS + \int_{f=0} \left[ \frac{\rho_0 v_n}{r^2(1 - M_r)^3} [r \dot{M}_r + c(M_r - M^2)] \right] dS, \quad (4)$$

$$p'_L(x, t) = \frac{1}{c} \int_{f=0} \left[ \frac{\dot{l}_r}{r(1 - M_r)^2} \right] dS + \frac{1}{c} \int_{f=0} \left[ \frac{l_r(r \dot{M}_r + c M_r - c M^2)}{r^2(1 - M_r)^3} \right] dS \\ + \int_{f=0} \left[ \frac{l_r - l_M}{r^2(1 - M_r)^2} \right] dS. \quad (5)$$

The variables are considered in the retarded time and the subscripts are related with the direction of the respective variable.

For the loading noise calculation, a chordwise compact loading distribution can be considered without affecting significantly the results<sup>12</sup>, reducing the computer power and time required in the calculation.

## 2.4 Kirchhoff Ffowcs-Williams Hawkings Formulation

The formulation 1A of Farassat, despite its recognized advantages in the calculation of rotor noise at subsonic conditions, does not address the quadrupole term responsible for the HSI noise. For that reason, the Kirchhoff Ffowcs-Williams Hawkings (KFWH) formulation was also implemented in the acoustic tool used in this work, in order to prepare it to analysis in which the quadrupole contribution is important. This method is a combination of the Kirchhoff method and the FW-H equation.

Both in the Kirchhoff and KFWH methods the integration surface is fictitious and penetrable, and the nonlinear effects can be considered by the surface integral with a careful placement of this permeable surface, that should be far enough to the rotor disk to surround the nonlinear flow region<sup>13</sup>.

The Kirchhoff method is valid for any phenomenon governed by the linear wave equation, and the FW-H is specialized for acoustics problems. As a consequence, the Kirchhoff equation requires further

information, provided by the pressure normal derivative  $\partial p/\partial n$ , requiring substantial computational resources.

The FW-H equation can be written as Eq. 6, considering that there is fluid flow across the fictitious surface.

$$\square^2[c^2(\rho - \rho_0)] = \frac{\partial}{\partial t}[\rho_0 U_n \delta(f)] - \frac{\partial}{\partial x_i}[L_{ij} n_j \delta(f)] + \frac{\partial^2 T_{ij}}{\partial x_i \partial x_j}, \quad (6)$$

where

$$U_i = u_i + [(\rho_0/\rho) - 1](u_i - v_i), \quad (7)$$

$$L_{ij} = p'_{ij} + \rho u_i(u_j - v_j). \quad (8)$$

Solving Eq. 6 in a similar fashion as the one used in the derivation of formulation 1A of Farassat from the impermeable FW-H equation, one can obtain:

$$\begin{aligned} 4\pi p' = & \int_S \left[ \frac{\rho_0 (\dot{U}_i n_i + U_i \dot{n}_i)}{r|1 - M_r|^2} \right] dS + \int_S \left[ \frac{\rho_0 U_i n_i K}{r^2|1 - M|^3} \right] dS + \frac{1}{c} \int_S \left[ \frac{\dot{F}_i \hat{r}_i}{r|1 - M_r|^2} \right] dS \\ & + \int_S \left[ \frac{F_i \hat{r}_i - F_i M_i}{r^2|1 - M_r|^2} \right] dS + \frac{1}{c} \int_S \left[ \frac{F_i \hat{r}_i K}{r^2|1 - M_r|^3} \right] dS, \end{aligned} \quad (9)$$

where

$$K = \dot{M}_i \dot{r}_i r + M_r c, \quad (10)$$

$$F_i = L_{ij} n_j. \quad (11)$$

## 2.5 Trailing edge noise

Broadband noise is a limitation in noise reduction due its difficult prediction. That fact is particularly noticeable in rotors and propellers, which generate broadband noise at the trailing edge. Trailing edge noise prediction is a challenge due to the complexity of the turbulence nature of the noise source, a fact that led to the development of prediction methods that use simplified turbulence models<sup>14</sup>.

Trailing edge noise is associated with the interaction of turbulent eddies formed within the boundary layer over the airfoil surface with the trailing edge. Trailing edge noise has a dipole nature with strength proportional to the fluctuating total force amplitude, scaling with  $M^6$ .

NASA developed two empirical models based on the boundary layer height at the trailing edge noise and the airfoil Reynolds number. In the present work the model developed was adopted for helicopter rotors by Schinkler and Amiet<sup>15;16</sup>. The peak Overall Sound Pressure Level (OASPL) is given by

$$OASPL = 50 \log(V/100) + 10 \log(\delta b/r^2) + 10 \log(\cos \phi \cos \theta/2)^2 + 113.9 dB, \quad (12)$$

where  $V$  is the relative velocity and  $\delta$  is the boundary layer thickness at the trailing edge, which can be calculated by

$$\delta = 0.37c(Vc/\nu)^{-0.2}. \quad (13)$$

The angles  $\phi$  and  $\theta$  are, respectively, the sideline angle and the direction angle relative to the chordline. The kinematic viscosity is represented by  $\nu$ .

The free-field 1/3 octave spectrum, relatively to the OASPL, in the absence of atmospheric attenuation can be represented as

$$SPL_{1/3} - OASPL = 10 \log\{0.613(f/f_{max})^4[(f/f_{max})^{3/2} + 0.5]^{-0.4}\}, \quad (14)$$

here  $f_{max}$  is the frequency at maximum amplitude, which is given by

$$f_{max} = 0.1V/\delta. \quad (15)$$

### 3 IMPLEMENTATION OF THE ACOUSTIC TOOL

The acoustic tool FACT (Farassat Acoustics CEIIA Tool), object of analysis in this work, was developed with the objective of simulating helicopter tonal noise, in steady and unsteady flight, in real-time.

FACT requires the blade loading distribution, the geometry of the rotors and the flight conditions as input. The aerodynamic loading can be distinct for each blade (a necessary condition for maneuvering noise) and it is interpolated to the correspondent blade position in each time step.

The rotor geometry is defined by the number of blades and rotors and as well as their relative position. The geometry of each blade is defined by a mesh input, taking into account the thickness of the airfoil, in order to calculate the thickness noise.

The movement of the rotorcraft is described by its linear velocity, initial position, attitude, rotor tilt angles and flapping and pitching coefficients. These parameters change in every time step in the case of unsteady flight, assuring a realistic simulation.

The acoustic integrals of formulations Farassat 1A and KFWH were numerically solved applying the source time-dominant algorithm. The integration surface is divided into  $N$  panels, each with area  $\Delta S_i$ , and the integral is evaluated at the centre of each panel,  $y_i$ , in the time of the source,  $\tau_e$ . Therefore, as illustration, Eq. 2 can be written as,

$$4\pi p'_T(x, t) = \sum_{n=1}^N \left[ \frac{\rho_0 \dot{v}_n}{r(1 - M_r)^2} \right]_{(y_i, \tau_e)} \Delta S_i + \sum_{n=1}^N \left[ \frac{\rho_0 v_n}{r^2(1 - M_r)^3} [r \dot{M}_r] + c(M_r - M^2) \right]_{(y_i, \tau_e)} \Delta S_i, \quad (16)$$

This algorithm was adopted because it is suitable to parallel computation and requires less arithmetic operations for maneuvering flight than observer-based integral methods. Since all panels have a different propagation time to the observer, the application of the source time-dominant algorithm results in an unequally spaced history of observer time point, requiring a interpolation procedure to sum the contribution of all panels in the same observer time. The interpolations do not take place at a constant pace, meaning that to the same time step most panels have a different number of interpolated values. One way to guarantee that all panels contribute to the total noise is to add the results only at the end of the simulation. However, this is not the best approach due to the amount of RAM required to keep the intermediate values. Therefore, instead of saving the data at the end of the simulation, FACT saves the results by segments of time, defined by the user at the beginning of the simulation.

Parallel computing plays an important role in the intermediate calculations: the CPU performs those calculations in series (one microphone at a time, panel by panel), but in the GPU those calculations are performed simultaneously. The device (GPU) does not have access to the host (CPU) data and vice-versa, so the variables for the noise calculation are transferred to the device and the results are then returned to the host, which implies an increase of RAM usage.

Using GPU programming is particularly advantageous for complex simulations because the time spent in transferring the data to the device is compensated by faster intermediate calculations. NVIDIA®'s CUDA C<sup>17</sup> was the GPU language adopted in the code.

Comparing the CPU and GPU versions of the code, one can notice that the advantages of the GPU version increase with the complexity of the problem (Fig. 1) and the RAM usage remains practically the same (Fig. 2), with a difference inferior to 200 MB.

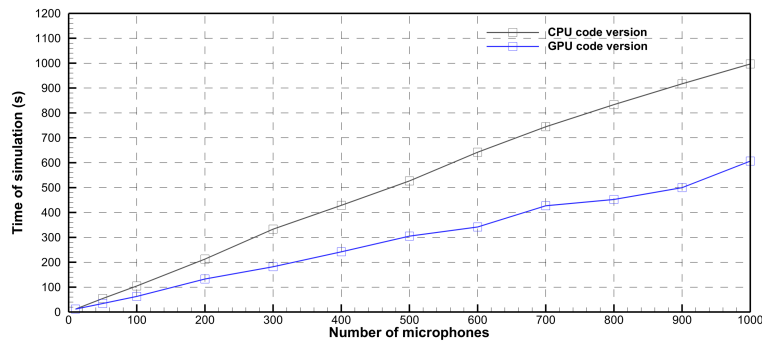
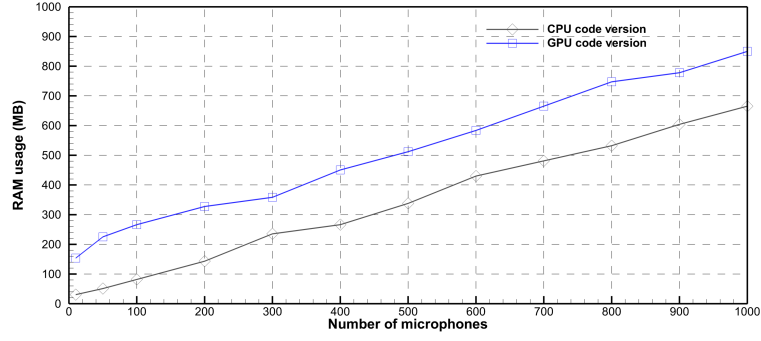


Figure 1: Comparison in time of simulation between the CPU and GPU versions of the code.



**Figure 2: Comparison of RAM usage in simulation between the CPU and GPU versions of the code.**

All results were obtained in a 64-bit Windows®7, with 8GB of RAM, an Intel®Core™i5 processor and a NVIDIA® Quadro K610M. The test case was a single rotor with five blades with the same mesh of 1800 panels, with a step in azimuth of  $2^\circ$  and 3000 iterations.

#### 4 EXPERIMENTAL PROCEDURE

In a first attempt of using FACT for modelling quadrotor UAV noise, model UX-SPYRO of UAVision was chosen; the model as well as its dimensions are given in Fig. 3, with the dimensions of Fig. 4.



**Figure 3: UX-SPYRO quadrotor.**

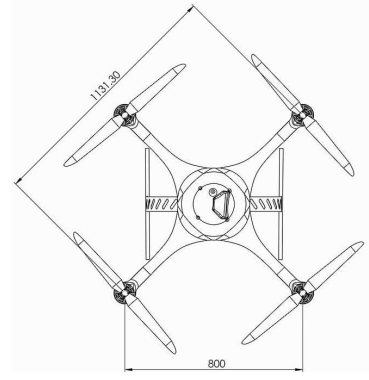


**Figure 4: Dimensions of the model (mm).**

Several experimental tests were conducted in the controlled environment of IST's Aero-Acoustic wind tunnel, using a single rotor of the UAV, as illustrated in Fig. 5.



**Figure 5: Experimental setup in the anechoic room.**

This first correlation between experimental and numerical results aims to identify the dominant type

of noise and the influence of the electric motor in the results, being a predecessor to the validation of FACT for the complete quadrotor in maneuvering noise.

Table 1 presents the angular speed of the four sets of measurements performed in the anechoic room.

**Table 1: Angular speed of the four experimental sets.**

#Set	Angular Speed (RPM)
1	225
2	1215
3	1905
4	2400

The noise was measured in three microphone positions at each set, in the coordinates given in Table 2.

**Table 2: Coordinates of microphone positions.**

Microphone	$x$ (m)	$y$ (m)	$z$ (m)
1	1.00	0.00	0.00
2	1.90	0.00	0.00
3	1.90	0.00	-0.60

The microphone positions 1 and 2 (with  $z$  coordinate equal to zero) are aligned with the rotor, and microphone position 3 is below the rotor disk.

## 5 NUMERICAL ANALYSIS

The computational chain used to analyse this problem is composed by two in-house software tools: FACT, here presented, and HFAST (Helicopter Full Aerodynamic Simulation Tool).

HFAST is an aerodynamic solver, which makes use of the Free Wake Method to represent the wake motion and its interaction with the lifting surfaces. This software also makes use of CUDA programming to accelerate the Free Wake routines, being able to analyse the lifting surfaces of generic configurations. Effects of viscosity, compressibility and Reynolds can be included through 2D profile C81 tables.

The only input data required for both FACT and HFAST are the quadrotor geometry and the operating flight conditions. In the case of HFAST, the input mesh must be the mid-surface of the blade, on the other hand FACT requires a more realistic mesh in order to take the thickness noise into account (Fig. 6).

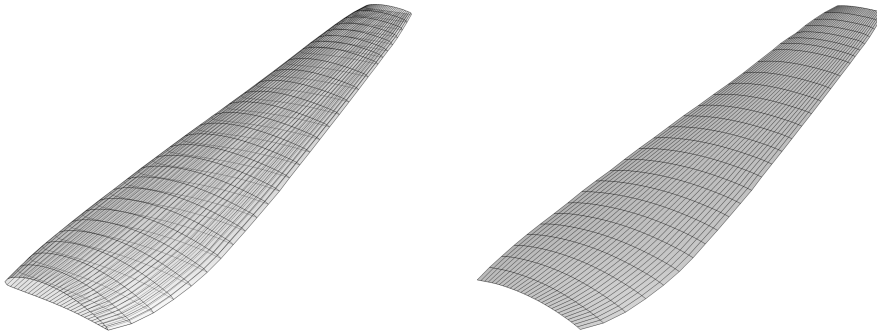


**Figure 6: Blade mesh of the quadrotor blade (at left) and mesh of the medium surface (at right).**

Fig. 7 and 8 demonstrate that the aerodynamic loading distribution is converged with a azimuth step of  $2^\circ$  for Set 3 and Set 4. The same was verified for all cases and therefore that was the value adopted in the numerical simulation.

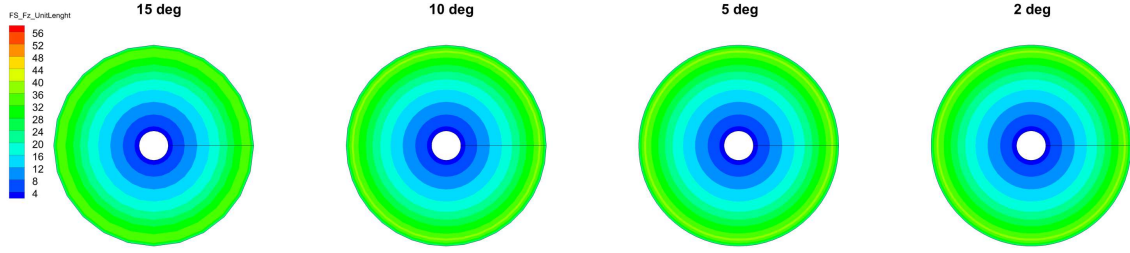


Figure 7: Aerodynamic loading distribution in the blade for different azimuth steps, Set 3.

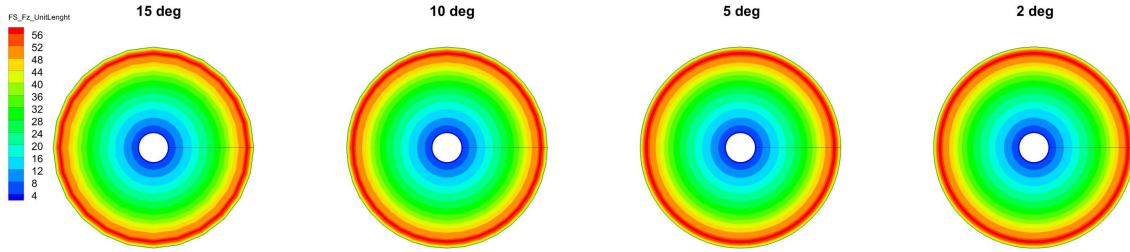


Figure 8: Aerodynamic loading distribution in the blade for different azimuth steps, Set 4.

In order to decide the interpolation step for the noise calculation with FACT, a study of convergence of the noise in Set 1 was performed in the time and frequency domains, represented by Fig. 9 and Fig. 10, respectively. The interpolation steps adopted are shown in Table 3.

Table 3: Values of interpolation step used in the study of convergence.

# Step	Interpolation Step (s)
1	1.50E-05
2	3.10E-05
3	8.00E-06
4	1.20E-04
5	2.40E-04

The results in the time domain are the same for all the different values of interpolation step. However, in the frequency domain, one can observe differences, particularly in the higher frequencies. Interpolation step 1 was therefore adopted for all the acoustic simulations.

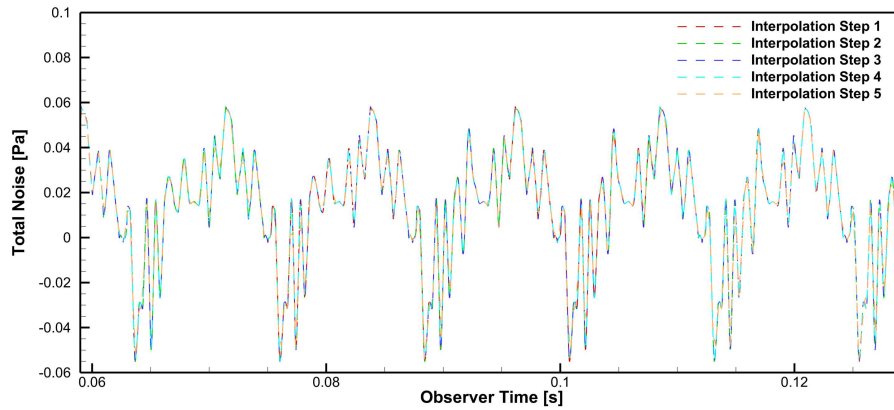


Figure 9: Convergence of acoustic pressure in the time domain for Set 1.



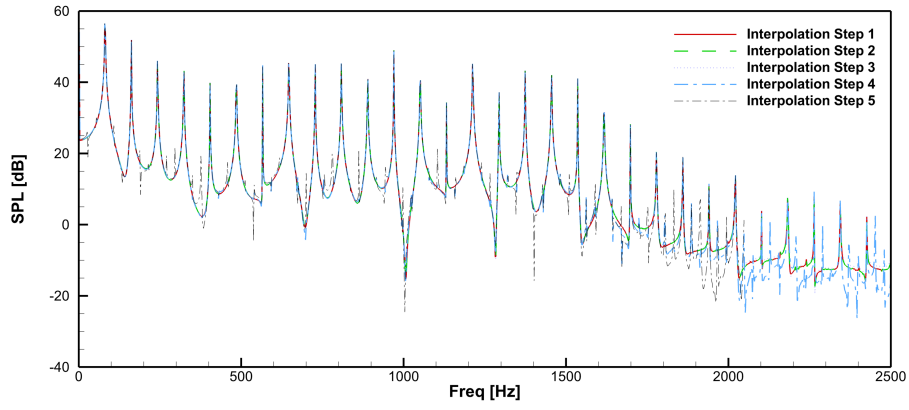


Figure 10: Convergence of Sound Pressure Level (dB) in the frequency domain for Set 1.

## 6 RESULTS

In order to have an analyse the interference of the background noise in the total noise spectrum, Fig. 11 and Fig. 12 show a comparison between the sound level spectra of the total noise and the background noise, for Set 1 and Set 2.

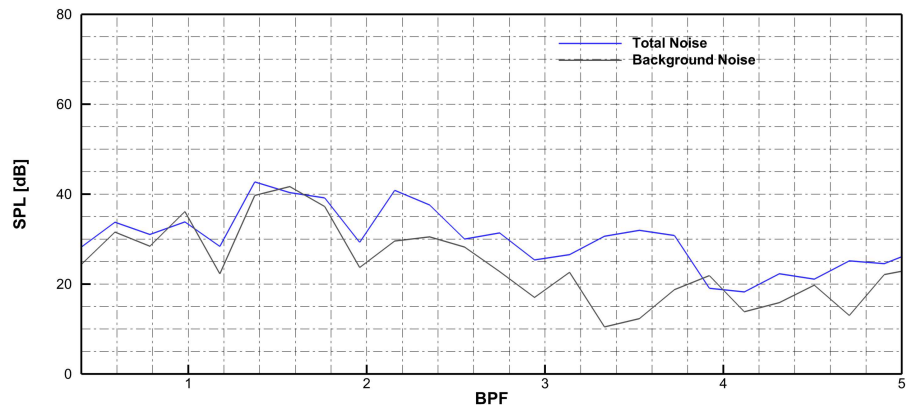


Figure 11: Comparison of total noise and background noise, for Set 1 in microphone position 1.

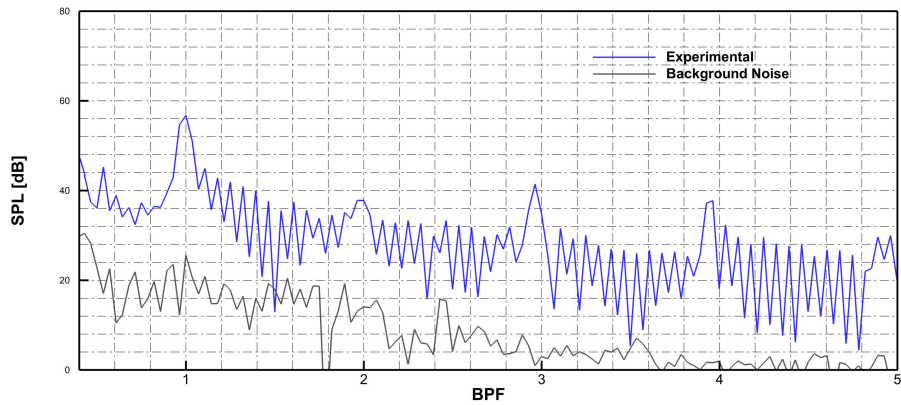
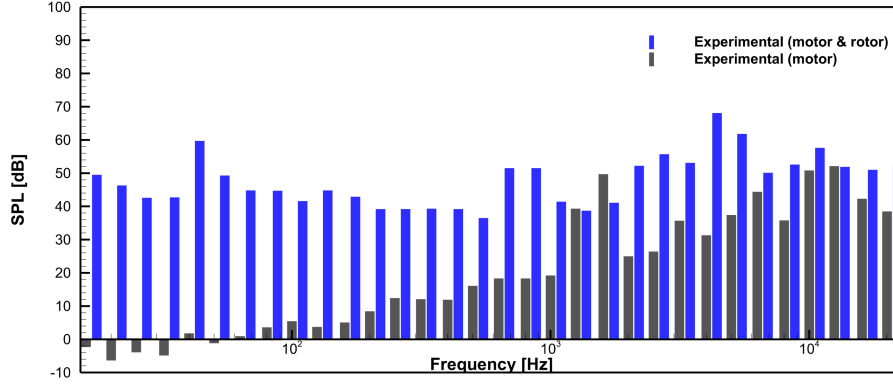


Figure 12: Comparison of total noise and background noise, for Set 2 in microphone position 1.

For Set 1, the background noise and the total noise have the same order of magnitude and for that reason this set of measurements will not be considered from now on. As the angular velocity increases, the background noise has a less significant contribution to total noise, as illustrated in Fig. 12.

It is also important to analyse the contribution of the electric motor to the total noise. If its contribution is more significant than the tonal noise, an optimization procedure will not reduce significantly the noise footprint on ground. Fig. 13 and Fig. 14 represent the 1/3 octave bands of the noise produced by the electric motor with no blades, when compared with the noise measured with blades included.

The acoustic behavior of the electric motor with and without the blades is not the same - these measurements aim to give an idea of the influence of the motor in the results.



**Figure 13:** Comparison of 1/3 Octave Bands, in dB, of the noise propagated from the electric motor and blades, and the electric motor, for Set 2.

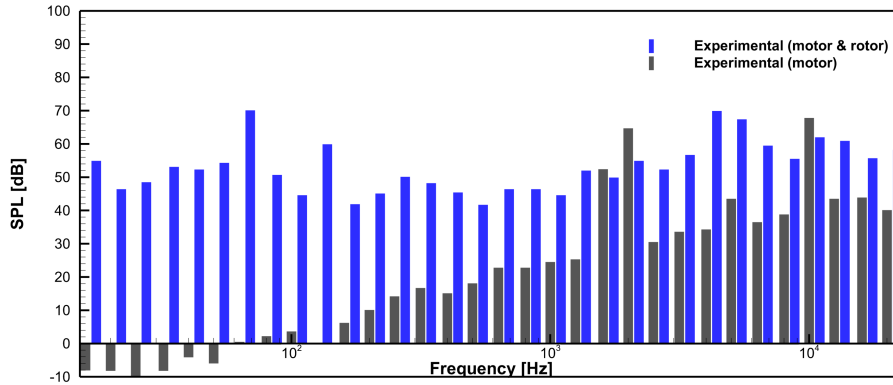


**Figure 14:** Comparison of 1/3 Octave Bands, in dB, of the noise propagated from the electric motor and blades, and the electric motor, for Set 3.

One can notice that the motor has a great influence in the higher frequencies of the noise spectrum; in some high frequencies the motor noise is even the only contribution to the total noise. For that reason, one should pay attention when correlating these frequencies to the numerical results.

The comparison and presentation of all measurements in the article would be exhaustive and would not add crucial information. For that reason only the most significant cases will be presented.

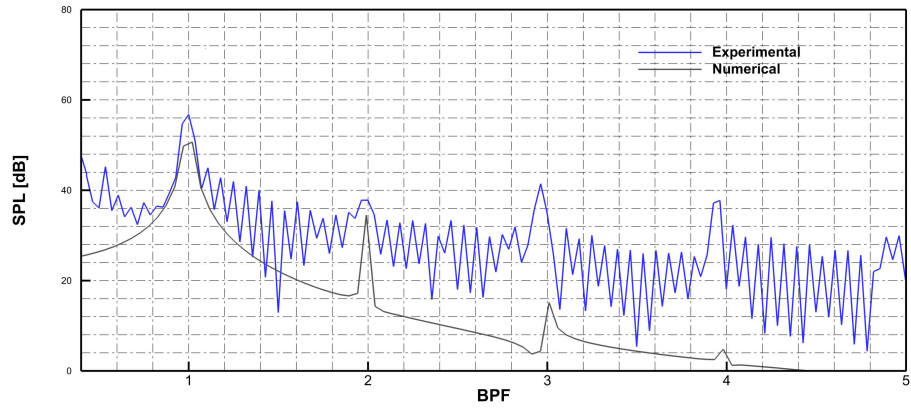


Figure 15: Numerical and experimental total noise spectra, for Set 2 in microphone position 1.

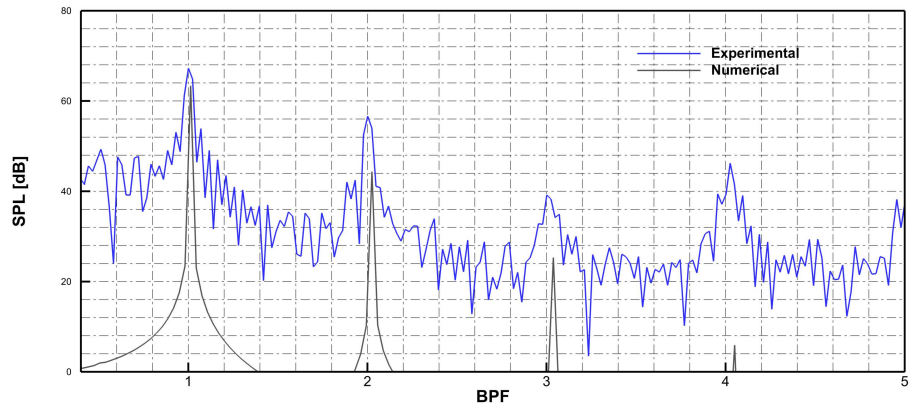


Figure 16: Numerical and experimental total noise spectra, for Set 3 in microphone position 1.

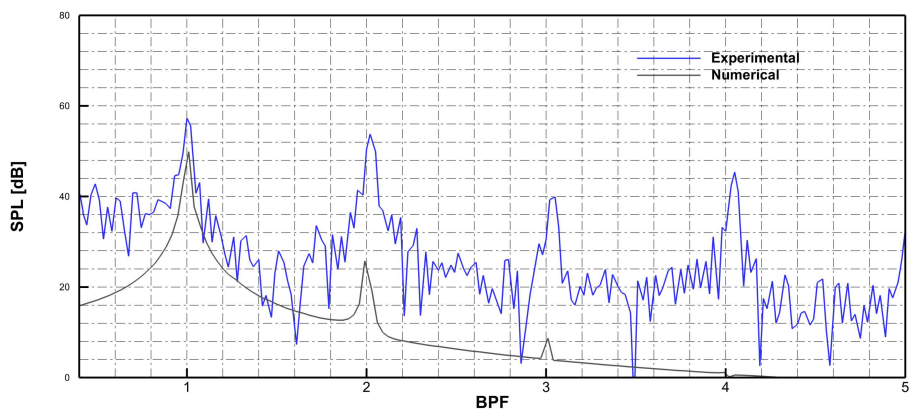
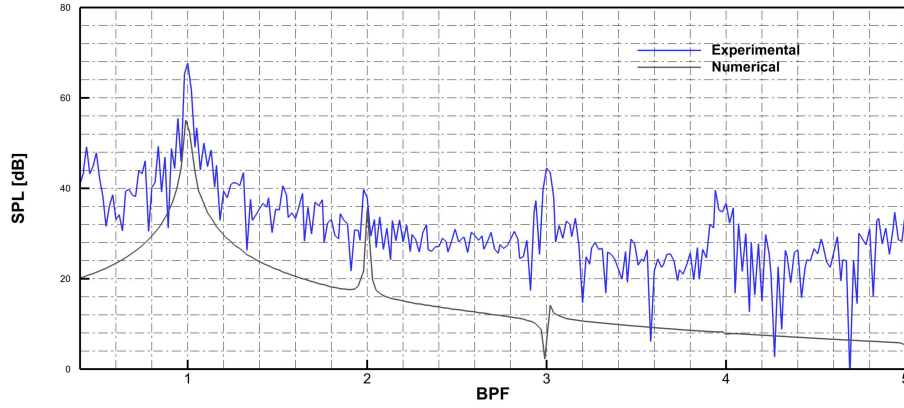


Figure 17: Numerical and experimental total noise spectra, for Set 3 in microphone position 2.



**Figure 18: Numerical and experimental total noise spectra, for Set 4 in microphone position 3.**

As can be observe in Fig. 15 to Fig. 18, the first peak of the harmonics is in agreement in the experimental and numerical results, and the same is true for the second peak in most cases.

Table 4 shows the values of OASPL (Overall Sound Pressure Level) for different frequency ranges, in order to illustrate that the results are closer when considering a limited range of frequency values, in which the most significant frequencies of background and motor noise are discarded.

**Table 4: Values of OASPL in dB, for all test cases.**

Set&Microphone	OASPL (16 - 20 000 Hz)		OASPL + TE Numerical	OASPL (40 - 1600 Hz)	
	Experimental	Numerical		Experimental	Numerical
2 , 1	70.6	54.3	55.4	61.8	54.2
2 , 2	67.7	39.5	49.0	52.8	39.5
2 , 3	65.9	36.4	48.7	54.5	36.4
3 , 1	75.4	63.5	64.6	71.0	63.5
3 , 2	70.1	51.5	58.9	63.0	51.5
3 , 3	71.9	50.1	58.8	64.3	50.1
4 , 1	82.2	68.4	69.4	77.4	68.4
4 , 2	73.7	57.5	63.3	67.9	58.3
4 , 3	76.2	57.9	64.2	71.6	57.9

As the angular speed value increases, one can observe a better agreement between experimental and numerical results due to the less significant interference of other sources of noise compared with the total noise. Therefore, the best correlation is obtained in Set 3 and Set 4.

The third column of Table 4 is the total noise with the contribution of an empirical formulation for the calculation of trailing edge noise, described in subsection 2.3. The trailing edge noise has a significant contribution in microphone positions 2 and 3 (far-field measurements), with a difference of 10dB in some of the cases, thus demonstrating the importance of broadband noise.

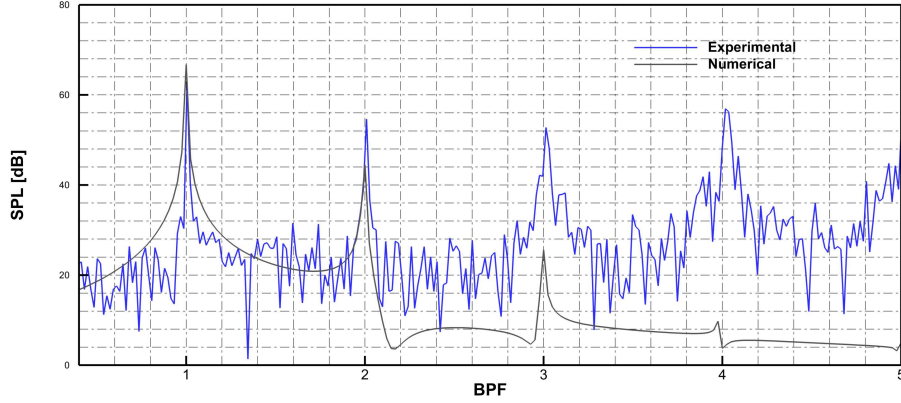
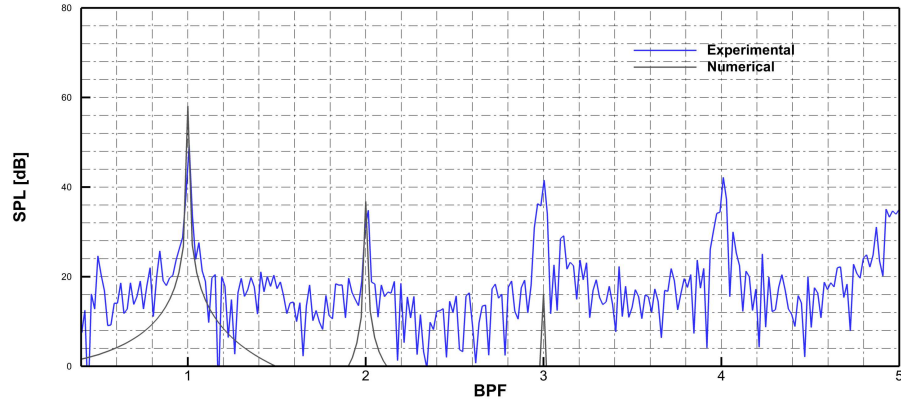
The worst results were obtained below the rotor disk plane. The tonal noise has a higher contribution in the direction aligned with the rotor because the thickness noise propagates mainly in this direction - the blade loading is axisymmetric and the loading variation is not high due to the hover flight conditions. Therefore, in the positions below the rotor, the motor noise and broadband noise contributions are more evident.

Several extra measurements were performed below the rotor disk plane, with the coordinates of Table (5); the angular speed was defined as in Set 3 and Set 4 since those were the values with better agreement with the numerical results and are also the more representative values during flight.

**Table 5: Coordinates of microphone position 4 and 5.**

#Microphone Position	$x(m)$	$y(m)$	$z(m)$
4	1.00	0.00	-0.25
5	1.90	0.00	-0.25

As representative data of those measurements, Figures (19) and (20) show the total noise spectra obtained numerically and experimentally for microphone position 5, at the angular speed of Set 3 and Set 4. The same analysis in terms of OASPL for these two new microphone positions can be found in Table (6).

**Figure 19: Numerical and experimental total noise spectra, for Set 4 in microphone position 4.****Figure 20: Numerical and experimental total noise spectra, for Set 4 in microphone position 5.****Table 6: Values of OASPL in dB, for Set 3 and 4, in microphone positions 4 and 5, in different frequency ranges.**

Set&Microphone	OASPL (16 - 20 000 Hz)		OASPL + TE Numerical	OASPL (40 - 1600 Hz)	
	Experimental	Numerical		Experimental	Numerical
3 , 4	74.6	61.3	63.0	69.1	61.3
3 , 5	66.3	50.6	58.6	55.3	50.6
4 , 4	79.0	66.9	68.5	75.5	66.9
4 , 5	70.1	58.2	63.4	63.4	58.2

In these new test cases, the experimental values of the OASPL are more in agreement with the numerical results than in microphone position 3; this was expected, since microphone position 4 and 5

are closer to the rotor plane than microphone position 3. The influence of trailing edge noise is more significant in microphone position 5. These results confirm the tendency observed in the first sets of measurements.

## 7 CONCLUSIONS

Through the comparison of the experimental results with the numerical results one can conclude the following:

- The tonal noise represents a significant contribution to the total noise and therefore there is room to advance to the optimization of the noise footprint on ground;
- The electric motor noise is very significant in the high frequency range;
- The trailing edge noise contribution plays an important role in the total noise.

Therefore, the computational procedure here presented proved to be adequate to the acoustic simulation of rotors with geometry and angular speed equivalent to quadrotor UAVs.

The introduction of trailing edge noise simulation in the acoustic tool, FACT, proved to be a valuable asset in this specific case of quadrotor noise, because it has a significant contribution in the total noise, demonstrating the importance of broadband noise.

The next step of this work is the noise simulation of the quadrotor UAV during maneuvers, in order to understand the effect of the interaction between rotors and rotors/fuselage during flight, as well as the influence of atmospheric effects.

## REFERENCES

- [1] K.S Brentner and F. Farassat. Helicopter Noise Prediction: The Current Status and Future Direction. *Journal of Sound and Vibration*, 170(5):79–96, 1994.
- [2] J. E. Ffowcs Williams and D. L. Hawkings. Sound Generation by Turbulence and Surfaces in Arbitrary motion. *Mathematical and Physical Sciences*, 264(1151):321–342, May 1969.
- [3] F. Farassat. The Kirchhoff Formulas for Moving Surfaces in Aeroacoustics - The Subsonic and Supersonic Cases. Technical Memorandum 110285, NASA, Langley Research Center, Hampton, Virginia, September 1996.
- [4] F. Farassat. Derivation of Formulation 1 and 1A Farassat. Technical report, NASA, March 2007.
- [5] F. Farassat. Linear Acoustic Formulas for Calculation of Rotating Blade Noise. *AIAA*, 19(9):1122–1130, 1996.
- [6] G. A. Brès, K. S. Brentner, G. Perez, and H. E. Jones. Maneuvering rotorcraft noise prediction. *Journal of Sound and Vibration*, 275:719–738, 2004.
- [7] S. Ianniello. Algorithm to Integrate the Ffowcs Williams-Hawkings Equation on Supersonic Rotating Domain. *AIAA*, 37(9):1040–1047, September 1999.
- [8] K. S. Brentner, G. A. Brès, Perez G., and H. E. Jones. Maneuvering Rotorcraft Noise Prediction: A New Code for a New Problem. Technical report, In Proceedings of AHS Aero- dynamics, Acoustics, and Test and Evaluation Technical Specialists Meeting, San Francisco, CA, January 2002.
- [9] Alex Stoll. Design of Quiet UAV Propellers. Master’s thesis, Stanford University, June 2012.
- [10] Giorgia Sinibaldi and Luca Marino. Experimental analysis on the noise of propellers for small UAV. *Applied Acoustics*, (74):79–88, 2013.
- [11] Kevin Massey and Richard Gaeta. Noise Measurements of Tactical UAVs. 2010.
- [12] K. S. Brentner, C. L. Burley, and M. A. Marcolini. Sensitivity of Acoustic Predictions to Variation of Input Parameters. *Journal of the American Helicopter Society*, 39(3):43–52, July 1994.
- [13] P. di Francescantonio. A New Boundary Integral Formulation for the Prediction of Sound Radiation. *Journal of Sound and Vibration*, 202(4):491–509, 1997.
- [14] C.J. Doolan. A Review of Airfoil Trailing Edge Noise and its Prediction. *Acoustics Australia*, 36, 2007.
- [15] Martin R. Fink. Minimum On-Axis Noise for a Propeller or Helicopter Rotor. *AIAA Journal*, 15(10):700–702, 1978.
- [16] Robert H. Schlinker and Roy K. Amiet. Helicopter rotor trailing edge noise. Contractor Report 3470, NASA, 1981.
- [17] NVIDIA®. CUDA C Programming Guide, July 2013.